# Influence of Interlayer Time on the Microstructural State of CoCrMo Coatings Applied by Selective Laser Melting on an Iron-based Substrate for Different Numbers of Layers

Tarek Younsi, Christine Boher, Adriana Soveja

# Influence of interlayer time on the microstructural state of CoCrMo coatings applied by selective laser melting on an iron-based substrate for different numbers of layers

Tarek Younsi [a,*], Christine Boher [a], Adriana Soveja [b]

[a] Institut Clément Ader (ICA), UMR CNRS 5312, Université de Toulouse, IMT Mines Albi, INSA, ISAE, UPS, Campus Jarlard, 81013 Albi, France
[b] Institut Clément Ader (ICA), UMR CNRS 5312, Université de Toulouse, IMT Mines Albi, INSA, ISAE, UPS, 3 Rue Caroline Aigle, 31000 Toulouse, France

A B S T R A C T

The Selective Laser Melting process was used to perform cobalt-based alloy coatings on a C35 steel substrate. The relationships between interlayer times, iron dilution, crystalline structures, and micro-hardness were studied for different numbers of layers with an initial lased powder layer of 50 μm thickness. Reducing the interlayer time increased the temperature reached in the melting bed and promoted matter transport from the substrate. The coating thickness consisted of a Co-Cr-Fe mixture, divided into two zones: a transition zone near the interface and a stabilized zone towards the substrate. The real coating thickness was found to be always greater when the interlayer time was reduced. For an interlayer time equal to 11 s (series 2), the iron dilution was always higher than for an interlayer time ranging between 42 s and 16 s (series 1), leading to a higher coating thickness. The microstructural state was also dependent on the interval time between successive layers. The coating microstructure was always cellular because of the high cooling rate. XRD analysis of the surface showed that this microstructure is essentially composed of two non-equilibrium phases: FCC and α' BCC. The high hardness is due to the high content of iron which induces a martensite phase (series 2). Starting from 5 layers for series 1 and from 6 layers for series 2, the α' BCC phase disappeared if the iron content on the coating surface was reduced by more than 45% content in weight. The mean coating hardness decreased with an increasing number of layers because of the decrease in the iron content. Finally, the micro-hardness of the FCC phase, for its part, was found to be dependent on the iron content in solution in the Co matrix.

## 1. Introduction

Cobalt-based alloys are often used as coatings on steel substrate to improve surface properties, such as corrosion and oxidation resistance, and also to improve wear resistance [1,2]. The most common cobalt-based alloy grades used in industry are CoCrMo alloys called stellites [2].

To apply CoCrMo coatings to the steel substrate surface, different depositing processes can be used, such as Metal Inert Gas MIG [3], laser cladding [4–6] or spraying processes [4]. During the CoCrMo alloy coating processes, iron dilution from substrate to coating can occur. This is due to the high input energy during these processes. The degree of dilution depends on the type of process and the input energy density, which is linked to the process parameters [3,4]. In order to characterize the behavior of samples, it is important to study this dilution of iron since it modifies the initial chemical composition of CoCrMo coatings and consequently the resulting microstructure.

It is well known that for MIG, laser clad and spraying processes, the microstructure of cobalt alloy coatings is made of dendrites surrounded by hard carbides [3–5,7].

Usually, the cobalt crystallizes on an FCC structure at a high temperature and on an HCP structure at room temperature. Because of the high cooling rate induced by quenching during the depositing processes, the crystalline structure of the CoCrMo coating remains FCC at room temperature. It can be transformed into an HCP structure after plastic deformation, because the FCC presents on out-of-equilibrium state. The FCC to HCP transformation is martensitic in nature and occurs without diffusion. It is known as plastic strain induced phase transformation.

The iron content also increases the stacking-fault energy, which has an influence on the plastic deformation mechanism of Cobalt alloys [8].

* Corresponding author.
*E-mail addresses:* tarek.younsi@mines-albi.fr (T. Younsi), christine.boher@mines-albi.fr (C. Boher), adriana.soveja@univ-tlse2.fr (A. Soveja).

There are several plasticity mechanisms involved in a Cobalt-based alloy subjected to mechanical stress, such as work hardening, which is the result of the gliding of crystalline planes translating into tangles of dislocations [9]. In addition, grain reorientation during mechanical solicitation produces texturing in the solicitation direction, which translates into the formation of planes of preferentially-oriented grains. For example, Cabrol et al. reported that the reorientation of grains occurs after tribological solicitation in the $< 111 >$ plane direction for FCC grains in the case of coatings produced by the MIG process [3].

Another type of additive manufacturing process, using powder bed technology, is Selective Laser Melting. This process uses high power to melt and fuse metal powder layer by layer. It is applicable to several grades of material powders. It provides very high accuracy in manufactured parts because of the small size of the laser spot and the layer thickness, which is usually between 20 and 100 micrometers [10].

However, the SLM process is usually employed to manufacture 3D parts on an industrial scale. Many studies have been conducted to understand the microstructural properties and mechanical behavior of CoCrMo alloy manufactured by the SLM process and their relationship with process parameters [11,12].

The main SLM process parameters, studied by different authors, impacting both the microstructural and mechanical properties of CoCrMo parts manufactured by SLM are: laser power, displacement speed, scan or hatch spacing, layers thickness and also the manufacturing strategy.

Laser power impacts material density, yield stress, tensile strength, elongation and wear rate. The power has an impact on the size of the melting bed and on the size of cells on the cellular microstructure [13–17]. Displacement speed has an influence on the density and mechanical properties of the part obtained. Its influence is linked to the applied power [13,16–18]. Scan spacing, or hatch spacing, influences the same properties [14,16–18], but it is reported in [14] that it has a lower influence on the final density than the power of the laser. Layer thickness plays a role in the size of both the melting bed and the microstructure [18]. The manufacturing strategy, including the direction of manufacture and the rotation angle of the laser track between successive layers, has an influence on the final properties of the material, such as fatigue life and tensile strength [14,19,20].

To describe the energy introduced during the process, one common formula is used [15,18]. It describes the density of volume energy during the SLM process as a function of the process parameters (Eq. 1):

$$E(J/mm^3) = \frac{P\ (W)}{v(mm/s).\ h(mm).\ s(mm)} \quad (1)$$

Where P is laser power, v is scan speed, s is scan spacing, h is layer thickness.

To the authors' knowledge, no scientific studies have been carried out on the case of coating applied by the SLM process on the substrate, or more specifically on the case of Cobalt-based alloy coatings on a steel substrate. Tan et al. [21] studied the interface between a Copper substrate and a maraging Steel part produced by SLM. Their study provides access to primary results dealing with the interface, where it was demonstrated that an interdiffusion region between iron and copper is created and that the thickness of this region is estimated to be 40 μm. Another study, by Chen et al., was carried out using SLM on the interface between 316 L steel an CuSn10 and showed that the interdiffusion thickness is about 600 μm [22].

The SLM process is carried out to perform cobalt base alloy coating on steel substrate. Using different fabrication conditions and for the same SLM parameters (ie scanning speed, laser power,…), the time interval between two successive layers can be varied even if the laser scanning time is equivalent for each layer. This work studies the effect of the time interval between two successive layers (ie inter-layer time) on iron dilution in the cobalt base alloy coating, the resulting microstructures and crystalline phases due to SLM process. The variation of iron dilution is also presented versus the coating thickness. EDX-SEM analyses are performed to estimate the iron content and XRD ones are used to identify the crystalline phases formed and the rate of each phase.

## 2. Material and methods

### 2.1. Sample manufacturing

The CoCrMo powder used in this study is a commercial product provided by SLM Solution. The particle size is in the range of 15 and 45 μm diameter, as specified by the supplier. The percentiles of this powder, as measured by laser particle sizing, are $D_{10}{}^{\frac{1}{4}}$ 15.95 μm, $D_{50}{}^{\frac{1}{4}}$ 29.77 μm, $D_{90}{}^{\frac{1}{4}}$ 53.69 μm. It can be noted that most of the particles are smaller than 50 μm in diameter. For this reason, the layer thickness will be 50 μm in this study, so as to include most of the particles in a single pass during SLM manufacturing. The chemical composition of the powder, according to SLM Solution's certificate, is shown in Table 1. The composition analyzed by EDX is also given in the same table. It can be noticed that the iron content in this powder is very low and considerably lower than 0.5% mass.

The SLM Solution (SLM125HL) was used with a 1070 nm wavelength Nd:YAG laser operating in continuous mode and delivering a maximum power of 400 W. The focus laser spot size ranged between 74 and 88 μm in diameter by default. The SLM parameters in this study are those recommended by the SLM Solution supplier (Table 2). The cross-hatching strategy defined in this study is that the scan direction rotates by 60° between two successive layers, so the laser track returns to the same direction every 3 layers. The rotations of the laser track direction between two successive layers are illustrated in Fig. 1. These conditions were the same for all fabrications and are very similar to those used by Tan et al. [21]. The hatching (or hatch distance) is the distance between two consecutive laser scan tracks. Some studies give hatching equal laser diameter [37] but others give hatching greater [13, 14] or less [11] than the laser diameter depending on SLM fabrication strategy. Literature explains when the laser spot is focused, the melt pool can influence neighboring 2–3 scanning tracks [37].

No post-treatments (thermal treatment or grinding or polishing) are applied on the samples after SLM process.

CoCrMo coatings were performed on 24 mm diameter and 10 mm high cylinders made of C35 unalloyed steel (Table 3). These cylinders were screwed directly onto a tray that had the same dimensions as the SLM build tray: 125 mm by 125 mm (Fig. 2.a).

Two series of SLM fabrications were performed to apply CoCrMo coatings to C35 steel. For each series, the parameter that changed was the number of layers, from 4 to 9, leading to a variation in the diluted iron content from the substrate to the coating surface. Fig. 2.a shows the location of each cylinder for each fabrication. Fig. 2.b shows the difference in the fabrication order between series 1 and series 2. The first series consisted of 6 cylinders fabricated on the build tray (the same fabrication). The sequence of building of each layer started identically on each cylinder and modified the number of layers for each sample. The second series consisted of only one cylinder per fabrication. Therefore, several fabrications were performed to obtain samples with different numbers of layers (Fig. 2.b).

Then, the interlayer time, which is the time between two successive layers, was estimated for each sample and each fabrication. For series 1,

**Table 1**
Nominal chemical composition of alloy powder used to make coating.

| Element | Co | Cr | Mo | Mn | Fe | Si | P | C |
|---|---|---|---|---|---|---|---|---|
| wt% SLM Solution Data | 63.45 | 28.90 | 6.40 | 0.30 | 0.20 | 0.60 | 0.04 | 0.11 |
| wt% EDS analysis | 62.86 | 28.32 | 6.12 | 0.93 | 0.46 | 1.36 | / | / |

**Table 2**
SLM parameters used in this study.

| Laser Power P (W) | Scan speed v (mm/s) | Hatching d (μm) | Layer thickness h (μm) | Rotation angle θ |
|---|---|---|---|---|
| 275 | 800 | 120 | 50 | 60° |

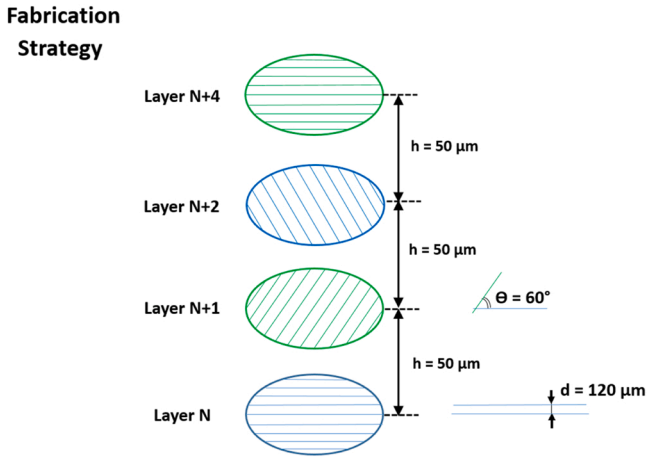


**Fig. 1.** SLM manufacturing strategy (example of 4 layers).

it decreased with the number of layers and was between 42 s and 16 s (Fig. 2.b). For series 2, the interlayer time was always the same, equaling 11 s. In the first case, the interlayer time is not constant because, in the manufacturing process, the laser first melts layer number N in all samples before moving on to layer N + 1. Between the fabrication of two layers "N and N + 1", the recoater applies a new powder layer. So, in series 1, as the number of samples involved in the fabrication decreases, the time required to apply a new layer is also reduced.

### 2.2. Sample investigations

First, the surfaces of all the coatings were examined. The iron content of the CoCrMo coating was measured by EDX-SEM analysis, considering the average value of 4 analyses. Each analysis was made using frames with dimensions of about 2 mm x 2 mm (Fig. 3). The thickness of electron penetration is estimated to 1–1,5 μm from coating surface.

To identify crystalline phases, the equipment used was a Philips

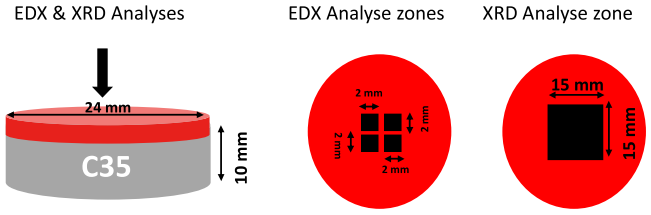


**Fig. 3.** Description of the analyzed regions for EDX analyses and XRD ones.

**Table 3**
Chemical composition of C35 steel according to certification.

| Element | Fe | C | Mn | Si | P | S | Cr | Ni | Mo | Cu |
|---|---|---|---|---|---|---|---|---|---|---|
| %weight | balance | 0,35 | 0,68 | 0,21 | 0016 | 0024 | 0,19 | 0,14 | 0,02 | 0,17 |

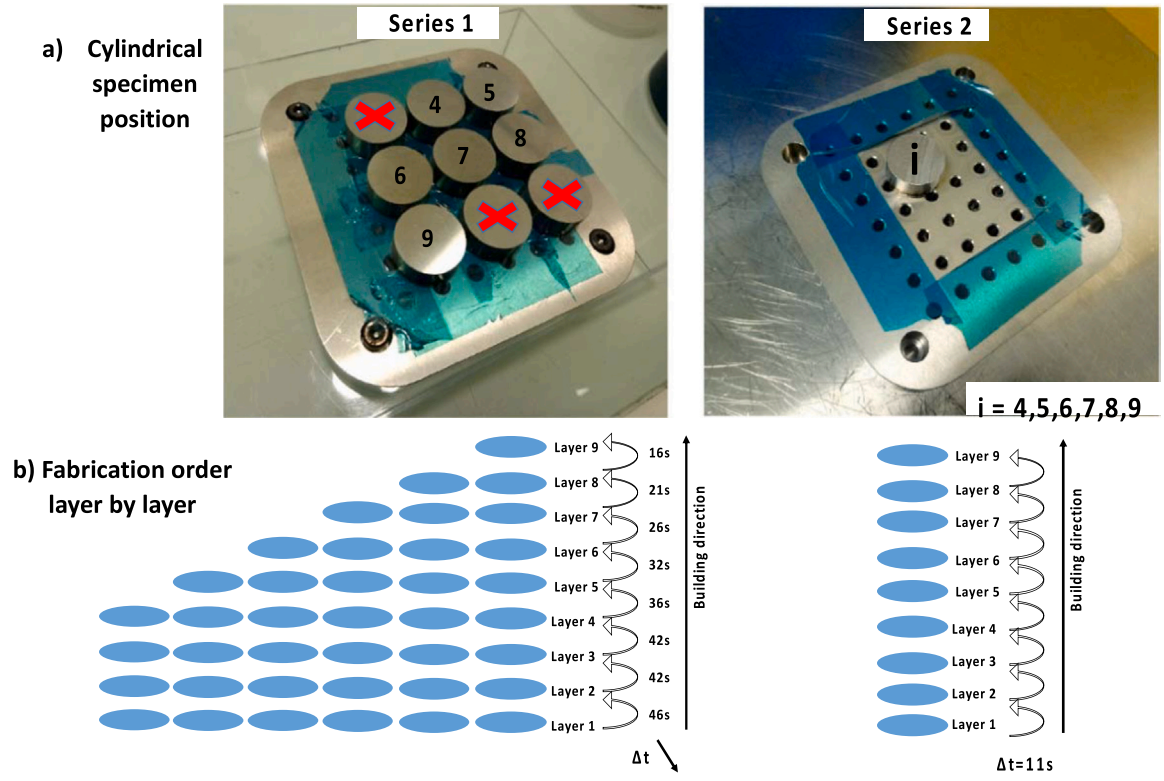


**Fig. 2.** Fabrication order: a) substrate cylindrical specimen position on the SLM manufacturing tray and b) fabrication order layer per layer for: Series 1: several specimens per fabrication - Series 2: one specimen per fabrication.

Panalytical XRD with an X′celerator detector using Cukα radiation. The dimensions of the frame analysis were 15 mm x 15 mm in the center of surface cylinder (Fig. 3). The XRD parameters were a voltage of 40 V, a current intensity of 45 mA and a step size of 0.033° with 200 s per step. The thickness of X-Ray penetration is estimated to 7 μm from coating surface. The XRD spectrum was obtained in which the intensity was plotted as a function of a 2θ scanning range between 25° and 100°. To estimate the phase rate, a post-treatment was required using the Relative Intensity Ratio (RIR) conventional method using High Score Plus software. This method calculates the ratio between the peak intensities of each phase averaged by the RIR value parameter of each phase.

To obtain a cross-section parallel to the build direction, including the substrate and coating thickness, all samples were sectioned along the cylinder in the direction of the laser lines on the coating surface, meaning the last layer. The samples were gradually polished with 180, 320, 600, 1200, 6, 3 and 1 μm grade papers. After polishing, they were chemical etched using a solution (60 ml HCl, 15 ml HNO3, 15 ml CH3COOH, 35 ml water) for a duration of 60 s

Microhardness tests were performed through the coating thickness from the coating surface to the bulk substrate using a BUHLER microhardness tester. A Vickers indenter was used with a 200gf loading. The spacing between two successive indentations was set to 110 μm. To evaluate the mean coating hardness, three tests for each sample were carried out: one in the middle, one at the sample border, and one in an intermediate position.

Finally, the cross sections were examined using a Hitachi Scanning

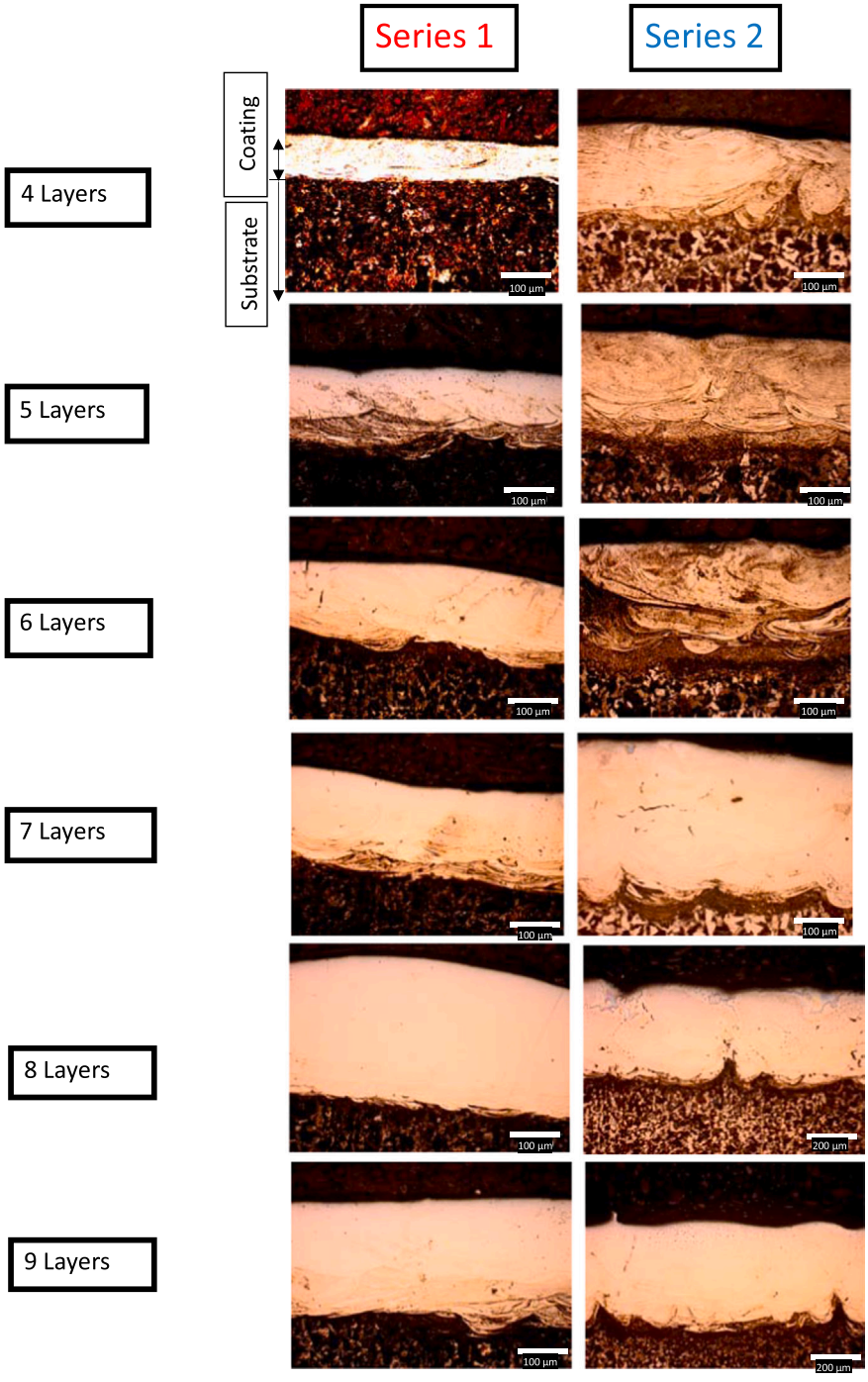


**Fig. 4.** Optical micrographs of samples of series 1 and series 2, showing the cross-section of the coating and the interface between coating/substrate.

Electron Microscope. To measure the iron content evolution along the thickness of the different coatings, EDX line scans from coating surface to coating/substrate interface EDX were performed. Three EDX line scans were made for each sample.

## 3. Results

### 3.1. Cross-section observations of coating

Optical observations of the coating cross-sections for each series are illustrated in Fig. 4. In this study, the rotation angle of the laser between two successive layers is 60 ° (Fig. 1 and Table 1), which means that in the cross-sectional observation only the third layer (melting bed) could be clearly observable. Coating thickness depends on the series. It is higher for series 2 than for series 1, but the difference decreases with the number of layers.

Considering the difference in interlayer times between the two series of fabrications, this first observation implies that the thermal flux is not the same for both series. When the interlayer time is low (series 2 with $\Delta t_l$=11 s), the temperature after fusing of each layer remains high, as explained in [23]. Consequently, the fused substrate thickness becomes more pronounced. We note that according to the literature, the laser thermally impacts up to ten layers, and can melt three underlying layers during its scanning [32,37]. Thus, for thin coatings, the coating composition could be a mixture of the iron element coming from the substrate and the chemical elements of the powder.

### 3.2. Coating thickness observations

The first observations show that the interlayer time during the SLM process strongly influences the thickness of the coatings, because these values are different between series 1 and series 2, as shown from the optical micrographs in Section 3.1. In this section, the estimated coating thickness will be compared using 3 different methods:

The first method uses a calculation drawn from the powder thickness, considering the theoretical powder layer and the filling density. This method, well explained in [24] and [25], takes into account powder density and considers only the fusion of powder without interdiffusion between substrate and coating. The real layer thicknesses are then calculated using the following equation:

$$h_l = \text{a}.h_{pow.theo} \quad (2)$$

Where "$h_l$" is the real thickness of the layer after laser fusion and solidification, "$h_{pow.theo}$" is the powder layer thickness before fusion (in our conditions $h_{pow.theo}$= 50 µm) which increases after the first layer because of metallic matter withdrawal. The value "a" is the filling density, which is the ratio between the powder density $\rho_{pow}$(=5.1 g/$cm^3$) and the density of the full dense material $\rho_{CoCrMo}$(=8.5 g/$cm^3$) [17,26].

It can be seen that the real thickness of the first layers "$h_l$" is less than the theoretical thickness "$h_{pow.theo}$". This is due to the density difference between the powder "$\rho_{pow}$" and the bulk material "$\rho_{CoCrMo}$", as explained in [24]. This difference particularly influences the heights of the first layers during the SLM process. It is reported in [25] that the layer thickness becomes very close to the theoretical thickness from the 7th layer. Thus, as the number of coating layers in this study is small (4 ≤ N ≤ 9), the real coating thickness obtained is very dependent on these first layer thicknesses.

The second method uses optical images from which the mean thicknesses are evaluated directly from 5 thickness measurements. The boundary between the coating and the substrate is identified as the end of the ferrito-perlitic structure, as shown in Fig. 5.a, in which only the case of 4 layers is shown. The boundaries between the substrate and the coating are clearly observed for both series.

The third method uses the evolution of the iron content determined by EDX line scans. The interface between substrate and coating is defined when iron content is close to 100%. The mean value of thickness is then obtained from 3 line-scans carried out on 3 different locations in

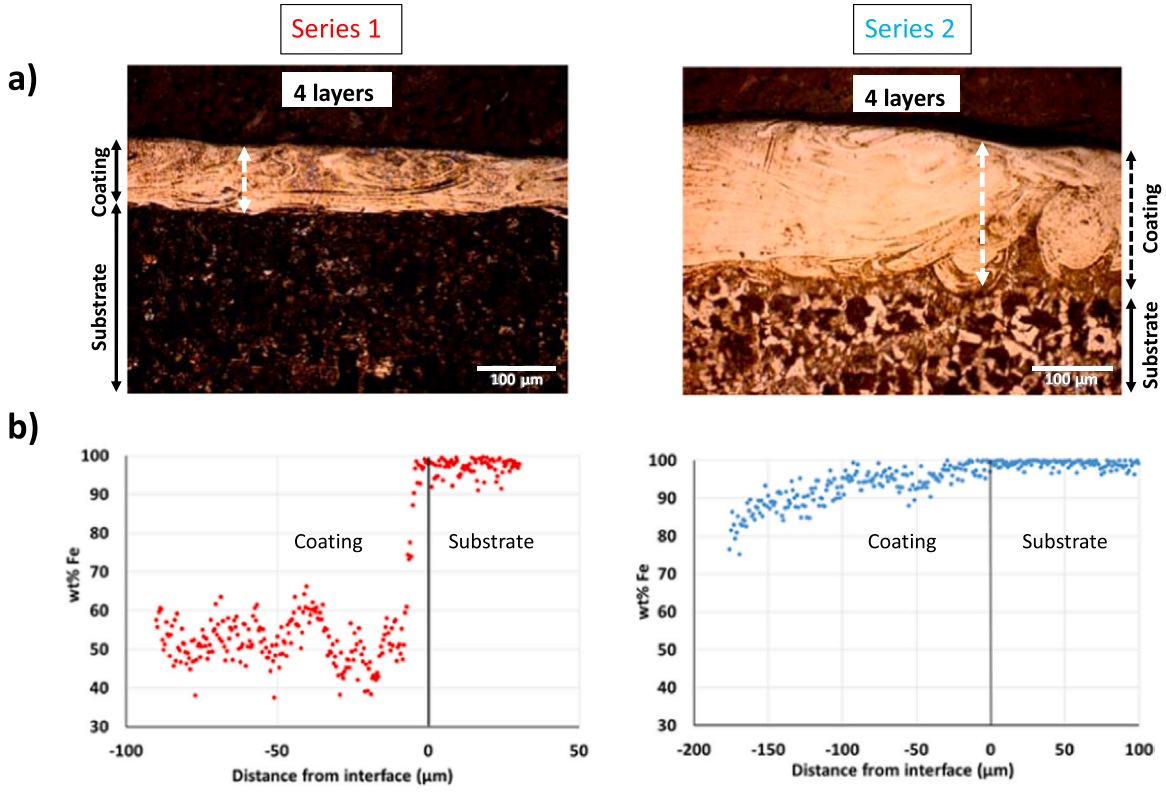


**Fig. 5.** Measurement of the coating thicknesses by 2 different methods: a) optical measurements, b) EDX line scan in the middle of sample (one represented among three).

the cross-section of the sample: one in the middle of sample and the others on the two sample extremities. One example is given, shown in Fig. 5.b for 4 layers of coating for both series.

The comparison between the methods for the two series is given in Table 4.

It can be noted that the thickness values obtained by the optical method are quite close to those obtained by the EDX line scan method and are significantly different from those obtained using the calculation method, especially for small numbers of layers. These results highlight that the thicknesses of the coatings differ significantly depending on the fabrication series, regardless of the number of layers (when this number is greater than 4). For an initial long interlayer time, as in series 1, the thicknesses are lower than for a short interlayer time. The thickness differences, in all cases, are in the range of 90–150 μm, which seems to suggest that it is the melting of the first layers that determines the total thickness of the coating. As the interlayer times are 42 s and 36 s respectively for layers 4 and 5 of series 1, melting occurs even in the substrate, the dilution of the chemical elements is significant but less pronounced than for low interlayer time and the thicknesses are lower. Finally, with the increase in the number of layers, the thickness tends to approach the theoretical value of the thicknesses for the results of series 2.

### 3.3. Iron dilution and crystalline phase analysis at coatings surface

For each series, the average content of iron at the coating surface is determined by EDX from rectangular areas (Fig. 3). The iron content (wt %Fe) is plotted as a function of the number of layers of coating (Fig. 6). In both series of fabrication, it can be observed that the iron content at the coating surface decreases with the increase in the number of layers.

In addition, the average iron content at the coatings surface is always higher for series 2, regardless of the number of layers. This could be due to a thermal effect, which is complex in the case of the SLM process because it involves several re-meltings of the laser, track by track and layer by layer.

As can be seen in Fig. 6, iron dilution at the surface decreases drastically (wt%Fe $< 10\%$) from the fifth layer in the case of series 1, while in the case of series 2, iron continues to dilute until the ninth layer.

In Fig. 7, the results of XRD analysis reveal the crystalline phases on the coating surface, which are reported for each series of fabrication. In Fig. 7-a and b, the crystalline phase amounts (in %) are represented by histograms and the iron weight content evolution by curves as a function of the number of layers for both series 1 and 2. In Fig. 7-c and d, the XRD pattern of the case of 4 layers is presented for each series.

By correlating the iron content with the crystalline phases present on the surface, it can be seen that two phases, FCC and α'-BCC (martensite), exist when the number of layers is low. In the case of series 1, both these phases exist only for 4 layers and a small HCP phase is also recorded for all numbers of layers. For series 2, α'-BCC (martensite) exists until layer number 5, but without an HCP phase.

The α'-BCC phase percentage is always greater for series 2 than for series 1. Starting from layers number 5 for series 1 and number 6 for series 2, the α'-BCC structure disappears. In this case, the structure becomes single phase (FCC) for series 2 and has two phases (FCC and a small HCP) for series 1 (Fig. 7).

An explanation of this crystalline state can be found by referring to the equilibrium phase diagram for Cobalt-Iron at a molar scale [27,28] shown in Fig. 8. The molar and weight phase diagrams of the binary Cobalt-Iron system are very close because of the very similar molar mass of the two elements ($M_{Fe}$=55, 84 g/mol, $M_{Co}$=58,93 g/mol) [29].

At the equilibrium state, the diagram shows that the microstructure presents two phases (FCC and BCC) only in a range of 8–22 at% Fe at 150 °C. The microstructure becomes FCC single phase at high temperature (T > 985 °C) with complete miscibility of each element in this phase. The microstructure is BCC in a range of 22–100at%Fe at room temperature [28].

The crystalline phases observed in this study do not correspond to the equilibrium state due to high cooling rates during the SLM process, resulting in an out-of-equilibrium microstructure, as explained in [30]. In the present study, the FCC phase is metastable and the resulting BCC phase is close to the martensite α'-BCC phase because of the high level of iron content and the high cooling rate, which leads to an incomplete diffusion process after cooling.

For this reason, in the case of 4 layers in which average weight iron content is 45% and 83% for series 1 and series 2 respectively, both the metastable FCC phase and the α'-BCC (martensite) phase are present, as shown in Fig. 7-a and Fig. 7-b.

A short interlayer time and a small number of layers lead to a high content of iron dilution through the coating. In this configuration, two phases are possible: the metastable FCC phase and the α'-BCC phase. This is clearly evident with series 2 for 4 and 5 layers because the interlayer time is only 11 s. For series 1, since the interlayer time is greater, the diluted iron content is lower through the initial layers.

### 3.4. Iron profile in coating thickness

To understand the evolution of iron dilution in the coating thickness, EDX line scans were performed through the cross-section of the coating, making it possible to compare iron content evolution between series 1 and series 2.

Fig. 9 presents the results of cobalt, chrome and iron weight content evolution performed by EDX line scans from the coating surface to the substrate in the case of 5 layers for both series 1 and series 2 respectively. This analysis shows that iron dilution content decreases from the interface substrate/coating to the coating surface and this dilution is always greater for series 2 than for series 1. Two zones can be observed: an almost stable zone and a clearly transient zone. It can be seen that iron content drops rapidly in the transient zone and stabilizes in the coating thickness. This phenomenon is observed in [31], where the author explains that this effect reflects a good dilution of elements in the inter-diffusion region.

In the case of the SLM process, the cooling rates are known to be high, and the temperatures reached are also sufficient to melt the powder and a part of the substrate volume, depending on the number of layers. This melting bed promotes matter transport, like iron atomic migration, from the substrate to the surface of the coatings [32]. It can be noted that the evolution of chromium follows that of cobalt, while iron seems to have the opposite evolution.

The evolution of the iron content by weight from the coating surface to the substrate is taken by EDX line scan for all cases. The profiles are shown for series 1 and series 2 in Fig. 10 for all numbers of layers (from 4 to 9). It can be noted that the iron concentration profile does not show

**Table 4**
Real coating thickness estimated by 3 methods: 1- powder layer thickness measurement. 2- EDX line scan. 3- Optical microscope measurement.

| | | 4 layers | 5 layers | 6 layers | 7 layers | 8 layers | 9 layers |
|---|---|---|---|---|---|---|---|
| 1- Calculations from layer powder thickness[24,25] | Thickness (μm) | 168 | 217 | 267 | 317 | 367 | 417 |
| 2- Optical microscopy measurements | Series 1 | 77 ± 8 | 138 ± 9 | 159 ± 9 | 182 ± 9 | 266 ± 12 | 250 ± 9 |
| | Series 2 | 185 ± 11 | 238 ± 10 | 249 ± 14 | 325 ± 18 | 373 ± 15 | 410 ± 17 |
| 3- EDX line scan | Series 1 | 80 ± 14 | 164 ± 14 | 172 ± 11 | 192 ± 2 | 290 ± 24 | 293 ± 21 |
| | Series 2 | 205 ± 21 | 224 ± 34 | 230 ± 71 | 337 ± 17 | 390 ± 57 | 445 ± 19 |

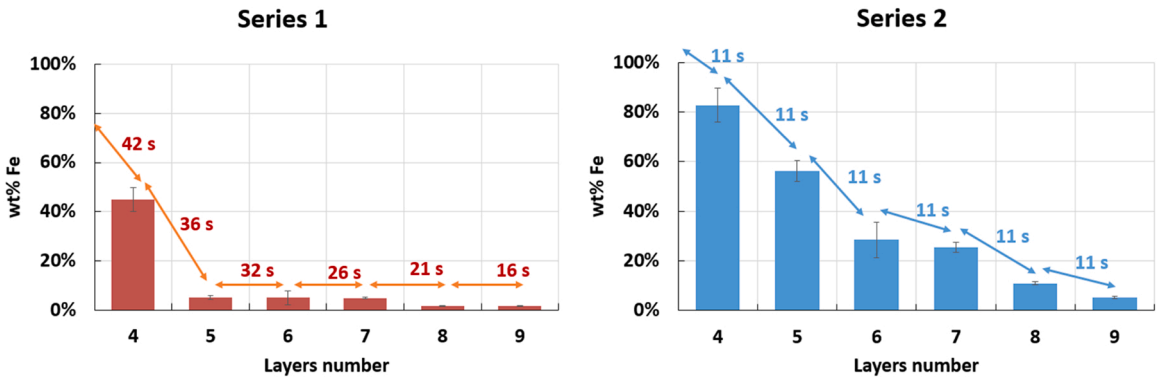


**Fig. 6.** weight content of iron at the coatings surface as a function of the number of layers of coating. Series 1: several samples per fabrication, Series 2: one sample per fabrication.

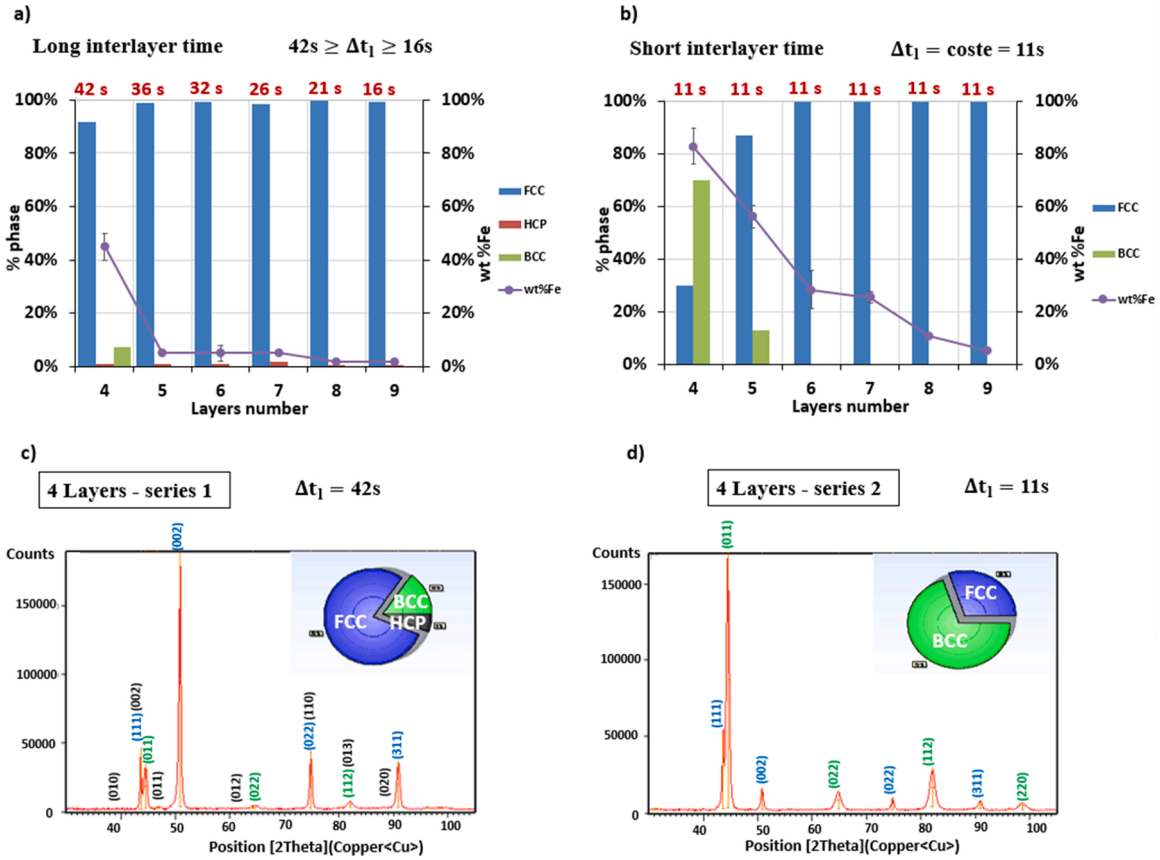


**Fig. 7.** Correlation between crystalline phase percentages estimated by XRD and Iron weight content estimated by EDX at the coating surface as a function of the number of layers of coating for the two series of fabrication. wt%Fe and crystalline phases for: a) Series 1; b) Series 2. Complete XRD pattern for 4 layers for: c) Series 1; d) Series 2.

the same pattern for different thicknesses of the coating. For a low number of layers, the iron content profile is rather constant over the thickness of the coating and the coating/substrate transition shows a very marked variation for series 1 and a more gradual variation for series 2, because the iron content is higher. The transition zone corresponds to a sharp increase in iron content before reaching the constant value of about 99.5%wt in the steel substrate. After 4 layers, the thickness of the transition zone is about 70–80 μm for series 1, whereas it can be more than 250 μm for series 2 because the iron content variation is more regular.

### 3.5. *Microstructure observations*

To understand the microstructural state indicated by EDX and XRD in Section (3.3) including crystalline phases and iron dilution in coatings, the cross-sections of all coatings were analyzed. A cellular microstructure (Fig. 11) was observed in the coatings for all samples of both series. In Fig. 12 the microstructure of 4 layers of coating is presented for series 1 and series 2.

The resulting cellular microstructure is coherent with the literature for CoCrMo alloys elaborated by SLM [13–15,18,19]. The fine cellular network is the result of a high cooling rate [33] which induces a non-equilibrium microstructure. This explains the existence of the

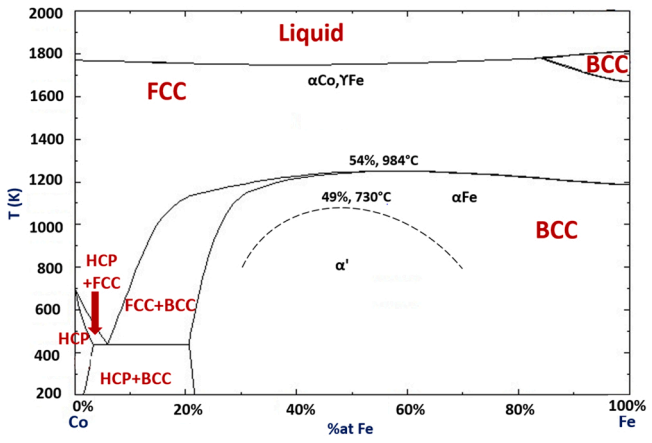


**Fig. 8.** Cobalt-Iron phase diagram [27,28].

metastable FCC structure at the coating surface, which exists only at high temperature, according to the cobalt-iron equilibrium diagram showed in Fig. 8.

For 4 layers of coating, two different microstructures are observed in the coating thickness (Fig. 12) for both series 1 and series 2. The two revealed phases react differently to the same etching solution (Fig. 12.a and Fig. 12.b). EDX analysis results for each phase are presented in Table 5. The more etched phase is richer in iron, so the resulting microstructure contains two phases with two different chemical compositions. According to the XRD analysis presented in Section (3.3), the two phases could be attributed to metastable FCC and α'-BCC structures. It is difficult to say which of the two observed phases is attributable to FCC and which to α'-BCC.

### 3.6. *Analysis of coating microhardness*

Since the crystalline phases and chemical compositions vary along the coating thickness from interface to surface, inducing microstructural changes, a variation of microhardness gradient is expected.

Microhardness is plotted along the cross-section of the coating, as shown in Fig. 13, where the profiles from coating surface to substrate in the cases of 4 and 9 coating layers are illustrated for both series. The analyses presented were performed in the middle of the sample. Similar trends are observed for all numbers of layers.

It is known that the microhardness of C35 steel substrate in the annealing state is about 190 ± 20 HV. It has been also verified that the microhardness of CoCrMo coating without iron is about 409 ± 31 HV.

In Fig. 13, for 4 layers, the evolution of the microhardness in the coatings is much higher than 190 HV (around 650 $HV_{0.2}$ and 350 $HV_{0.2}$ for series 2 and series 1 respectively), and, again for 4 layers, the level of iron content is up to 80% in mass for series 2. These results confirms that the BCC phase in series 2 represents a martensite phase and not a ferritic phase and thus has to be rewritten as α'-BCC.

For 9 layers, the evolution of the microhardness in the coating is lower than the average value of the microhardness of CoCrMo coating without iron (380 ± 28 for series 1 and 336 ± 21 for series 2). It is also noted that the level of iron content is less than 20% in mass and the phase is metastable FCC. These results indicate that small additions of iron decrease the hardness of the CoCrMo coatings.

In cross-section, the Heat Affected Zone (HAZ) corresponds to the region near the interface with high microhardness. It is the result of a quenched microstructure in the presence of very high iron content. In the case of 9 layers, it reaches 540 HV for series 1 and 600 HV for series

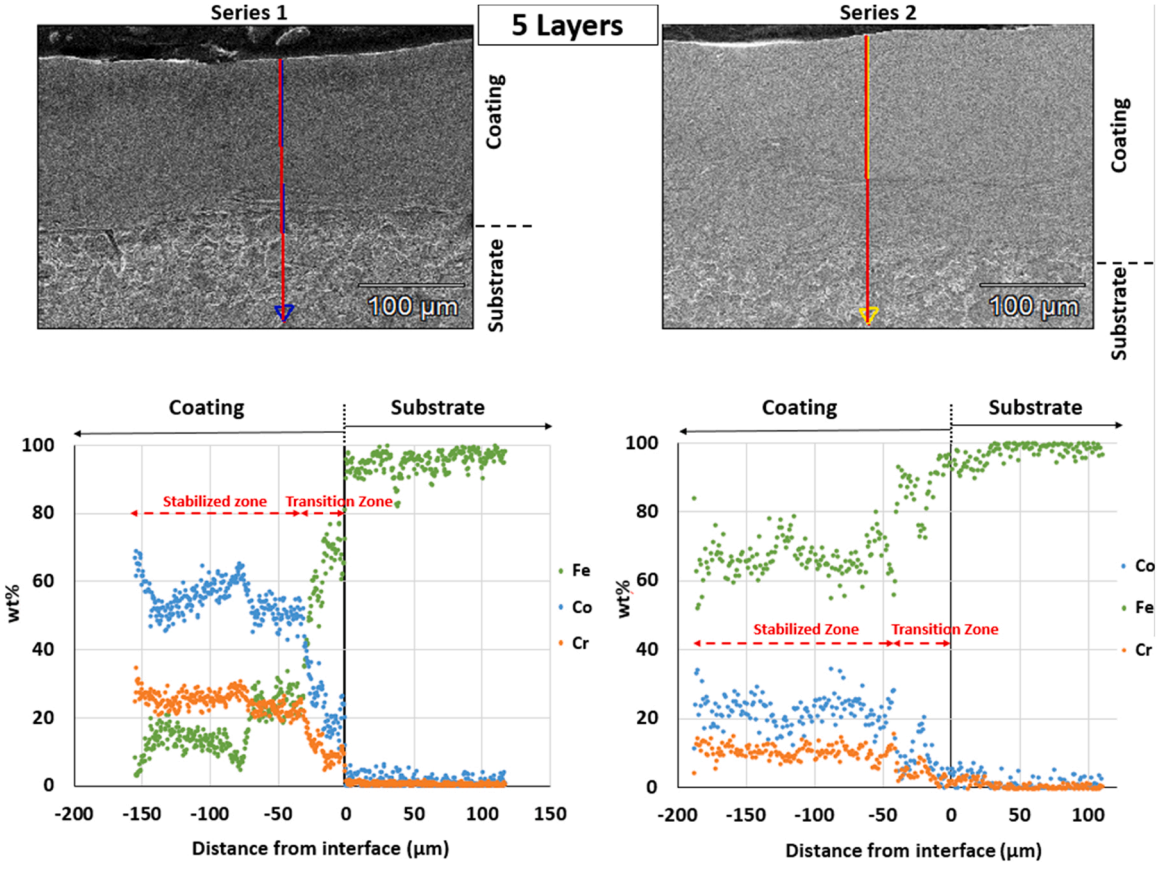


**Fig. 9.** Results of EDX line scans on coating thickness in the middle of sample in the case of 5 layers for series 1 and series 2: a) SEM images, b) Profiles of Iron, Cobalt and Chrome.

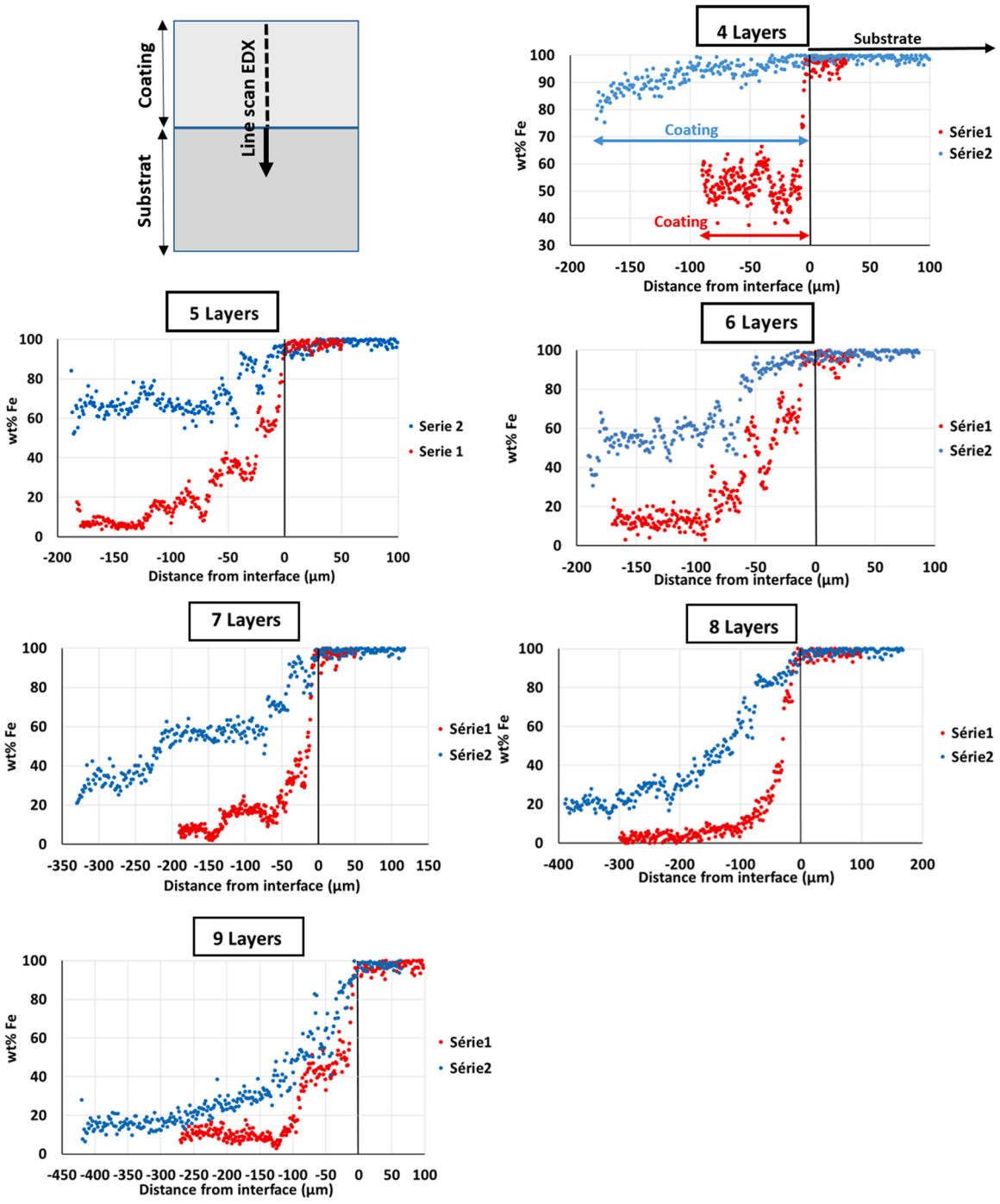


**Fig. 10.** Comparison between two series samples for iron weight content evolution on the coating thickness estimated by EDX line scan in the middle of sample in the cases of 4, 5, 6, 7, 8 and 9 layers for series 1 (red profile) and series 2 (blue profile).

2. It is higher for series 2 due to the iron dilution content, which is always higher in all series 2 coating thicknesses, as has already been shown in Fig. 10.

In Fig. 14, the mean microhardness of the coating (estimated from surface to interface excluding HAZ) is plotted as a function of the number of layers, in order to compare results between series 1 and series 2. The average coating microhardness value is estimated from 3 profiles performed in the coating thickness at three different locations.

The two series have different mechanical behaviors. The mean coating hardness (Fig. 14) from 4 to 9 layers remains approximately constant for series 1 whereas it decreases for series 2 before slightly increasing between 7 and 9 layers. The mean hardness is always higher for series 2 than for series 1 for 4 and 5 layers, whereas the opposite is true between 6 and 9 layers. The high level for 4 and 5 layers of series 2 is due to the high fraction of α'-BCC, which is very hard. From 6 layers, the coatings present only a single-phase FCC for both series and the mean hardness is always less than 409 HV (the mean hardness of CoCrMo). In this range, the higher the iron content, the lower the mean value of the hardness. For 9 layers, the mean coatings hardness starts to become close for the two series because the content of iron is also similar.

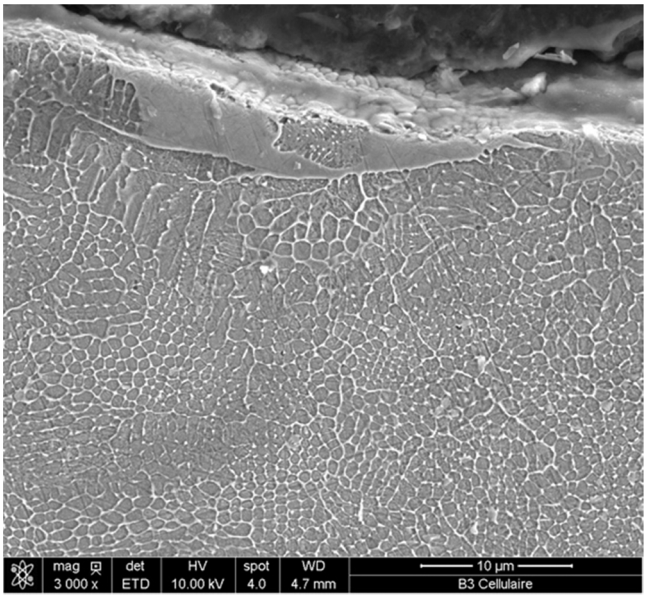


**Fig. 11.** SEM micrograph near surface of coating cross-section for 5 layers (series 2) showing two different phases at the extreme surface and cellular microstructure.

## 4. Discussion

The aim of this work is to compare the effects of two different strategies for the SLM manufacturing of CoCrMo coatings on steel substrate by influencing the interlayer time. The interlayer time is the total period of time for powder recoating plus the laser exposure time in layer N [23]. Results shows that the interlayer time impacts both iron content and crystalline phases and consequently influences coating micro-hardness.

The laser generates a high thermal energy input, equal to 57,29 $J/mm^3$ according to Eq. (1), which is in the range of the used energy value according to the literature, especially for CoCrMo SLM powder [15]. This high thermal energy causes the iron atoms to move, due to fluid movement and the Marangoni effect during melting. The Marangoni effect is the mass transfer between two fluids due to the surface tension gradient, which is crucial in the SLM process [34]. The iron content decreases when moving away from the coating/substrate interface. The migration of iron atoms is in the opposite direction to the thermal flux, from a high iron concentration zone to a low iron concentration zone, from the coating/substrate interface to the coating surface [9,35,36].

In a state-of-the-art review in [23], the authors affirm that higher cooling rates and higher temperature gradients are due to the longer time intervals between layers. Reducing the interlayer time increases the temperature reached in the melting bed [23] and promotes matter transport from the substrate. The authors prove with in-situ thermography that reducing interlayer time from 116 s to 18 s implies that IR-Signal values increase from about 440 to about 610 in layer number 2250 for a standard energy density (65,48 $J/mm^3$). In addition, during the multi-layer manufacturing process of selective laser melting (SLM), it is noted in the literature that the laser fuses not only the last powder layer but also previous layers, with temperatures reaching more than 2000 °C. In [32], the authors note with FE results that as layers increase, the maximum temperature, dimensions and liquid lifetime of the molten pool also increase, while the cooling rates decrease.

In this work, the coating thicknesses of series 1 are always lower than those for series 2 (deviation of 100 µm), and for series 2 the interlayer time is constant and short ($\Delta t_l$=11 s) compared to series 1 (42 s > $\Delta t_l$ >16 s). In addition, for series 2, the real coating thicknesses are close to those calculated by the powder layer calculation method. This large deviation in thicknesses between the two series could be due to thermal flux, which is greater for series 2 because of the reduced interlayer time [23]. The short interlayer time increases the temperature reached during laser melting, increasing the thickness of the melted substrate during the manufacturing of the first layers and consequently the transport of matter from substrate to coating. For a same number of layers between the two series, when the dilution of the iron is higher, the thickness is also higher. This can be attribute to the principle of conservation of mater (mass conservation) for cobalt element. This agrees with optical observations presented in Fig. 4.

This transport of matter leads to higher coating thicknesses, and it is in good agreement with the present work because the difference between theoretical and real values decreases as the number of coating layers increases for series 2 ($\Delta t_l$=11 s).

In the SLM process, the laser remelting between successive layers must be taken into account, because the laser impacts several underlying layers [32,37], thus increasing iron dilution to the surface. On the other

**Table 5**
Results of EDX (%wt Fe) analysis by shot frames in different areas of 4 layers coatings: a) series 1, b) series 2.

| a) | | | | b) | | | |
|---|---|---|---|---|---|---|---|
| | %Fe | %Co | %Cr | | %Fe | %Co | %Cr |
| Pt 1 | 55.16 | 27.06 | 12.31 | Pt 1 | 82.94 | 9.02 | 4.45 |
| Pt 2 | 8.84 | 58.17 | 26.24 | Pt 2 | 33.67 | 40.73 | 19.61 |
| Pt 3 | 64.16 | 22.20 | 10.08 | Pt 3 | 35.40 | 41.10 | 17.92 |
| | | | | Pt 4 | 83.45 | 9.14 | 4.35 |

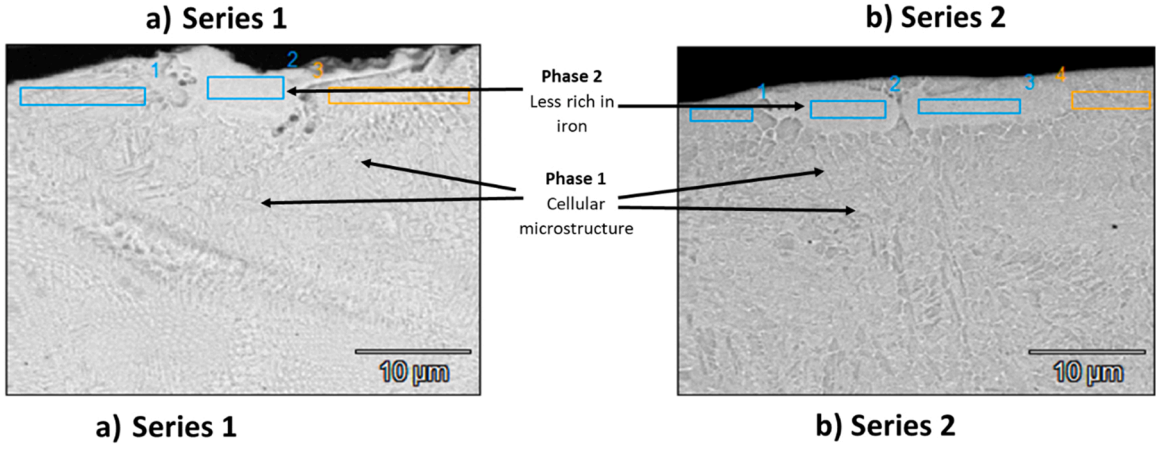


**Fig. 12.** SEM micrographs near surface of coating cross-section for 4 layers and EDX analysis by shot frames in different areas of coating, showing two different phases. a) Series 1; b) Series 2.

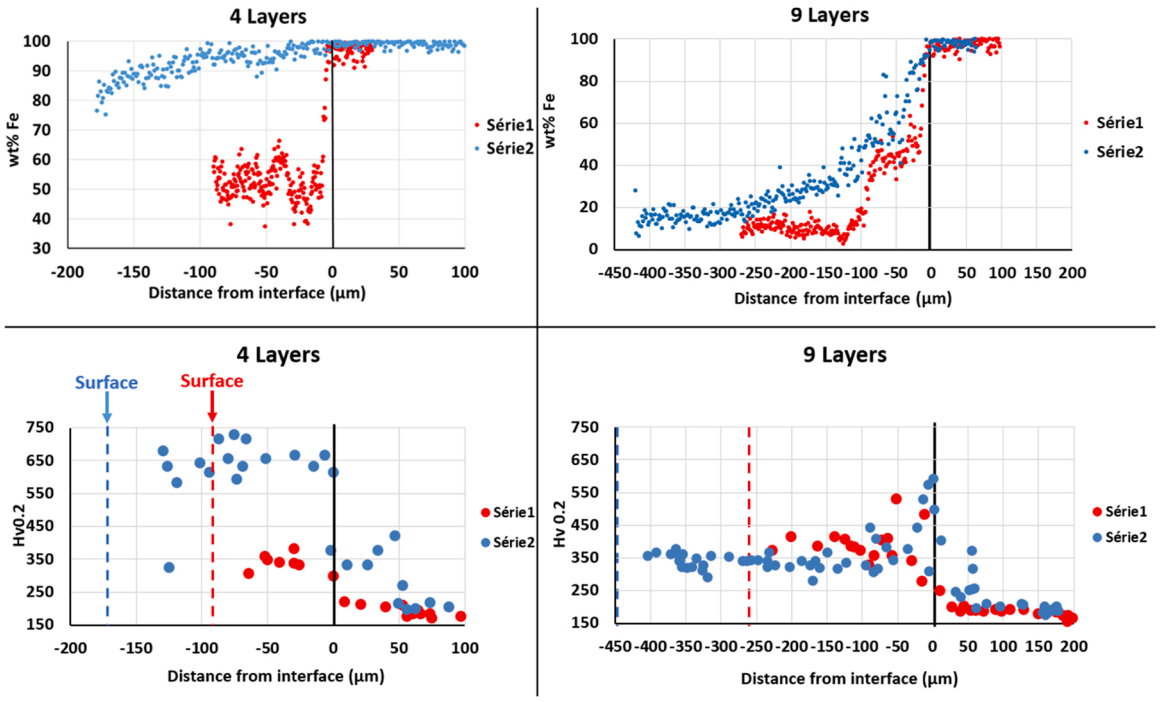


**Fig. 13.** Comparison between microhardness profiles performed in the middle of coating layers 4 and 9 for series 1 and series 2, correlated with iron EDX profiles.

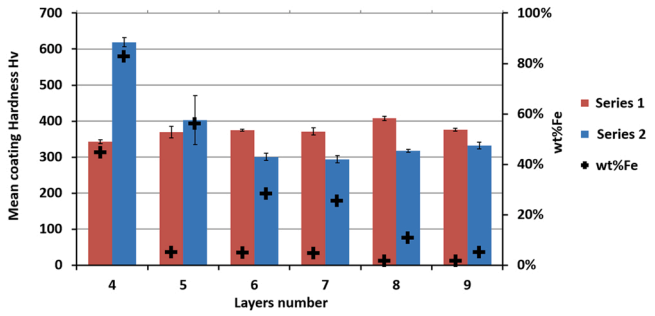


**Fig. 14.** Comparison between the average microhardness of coatings between series 1 and series 2.

hand, for a same number of layers, the dilution of iron in the coating is higher for series 2 than for series 1 (Fig. 6). Indeed, for series 2, the larger dimensions of the melting bed and the lower cooling rate lead to a higher dilution of iron from the substrate to the coating surface. Iron dilution in the coating is greater because the thickness of the fused substrate becomes more significant. Reducing interlayer time promotes matter transport from the substrate and consequently leads to the dilution of iron.

In this work, iron atoms are present up to the coating surface and the coating thickness is divided into two different zones: a stabilized zone which represents the Fe-Co-Cr mixture zone after melting, and a transition zone near the interface, known as the dilution zone (Fig. 9). It is reported in [39], for the laser cladding process, that iron is diffused from the substrate until 130 µm thickness, corresponding to a distance of 560 µm from the coating surface; After that it stabilizes, and the distribution of elements becomes homogenous. Thus, the shape of the iron content curve presented in [39] is comparable to the evolution of iron content in the present study, since it decreases gradually towards the substrate in the dilution zone and tends to stabilize through the interface. The authors consider that this result is caused by the melting of the substrate surface along with the melting of the powder mixture combined with melt pool convection. Furthermore, when dilution of iron is possible until the coating surface, the whole Fe-Co-Cr mixture zone, including the transition and stabilized zones, represents the coating.

To explain the crystalline phases of the coating, according to Fig. 7, for 4 and 5 layers of series 2, the resulting state is two substitutional solid solutions of iron in cobalt or cobalt in iron, because of the very similar atomics radii of these two elements, which are 2.37 Å and 2.33 Å for iron and cobalt respectively [38]. The resulting metastable FCC structure for a CoCrMo alloy performed by SLM is very common in the literature because of the high cooling rate, which results in a retained FCC structure at room temperature [11,14,19]. For other processes used for CoCrMo coatings on a steel substrate, like MIG, laser or PTA, the resulting structure is also metastable FCC. This is the case even where the iron dilution occurs up to the coating surface, as recorded for the MIG process (30.73 wt%Fe in [3]) and for laser cladding (11.8 wt%Fe in [4]).

Due to the high iron content (≥45%wt), the BCC phase appears on the surface of the coating in addition to the FCC phase, with 4 layers for series 1 and up to 5 layers for series 2. For more layers, the BCC structure disappears as the iron content decreases. It is also noted that a small amount of HCP phase is still present in series 1. Considering the Iron-Cobalt equilibrium diagram [27,28], HCP is possible - by a diffusion mechanism - only in the case of a very low cooling rate after the transformation of BCC into HCP.

Two hypotheses could be formed for the HCP phase presence before any mechanical solicitations:

- For series 1, the temperature reached is lower and the cooling rate is higher, according to [23]. This information could imply that the temperature reached after cooling between successive layers is lower and thus below the FCC-HCP transition (T° between 160 °C and 410 °C) (Fig. 8), which may explain the appearance of a low HCP content. This could be consistent with the current results for a longer interlayer time.
- Another way to explain the observation of the HCP phase on the surface of the Series 1 coatings is that higher cooling rates lead to mechanical stresses that could be significant and induce a transformation of the FCC phase into the HCP phase.

In addition, the iron prevents the FCC to HCP transformation in a Cobalt-based alloy during cooling. As observed in Fig. 8, according to the Cobalt-Iron phase diagram, the apparition of the HCP phase is possible only if the iron weight content is lower than 22%. For series 2, the iron content is greater than it is for series 1, exceeding 22% for ($N \leq 7$), which might explain the prevention of the transformation of the FCC phase to HCP.

The XRD technique, when performed on the coating surface, doesn't distinguish between Body Centered Cubic (BCC) peaks and Body Centered Tetragonal (BCT) peaks, which correspond to martensite α'. Thus, in the case of 4 layers for series 2, the high hardness in the coating, reaching 728 HV, can be attributed to a BCT phase, instead of a BCC structure, which can be detected by XRD. The BCC phase can be rewritten martensite α'BCC. Consequently, as shown in Fig. 13, it can be supposed that martensite α'BCC is also present near the interface in the transition zone (near the interface, known as the dilution zone (Fig. 9) for the 9 layers case, where the hardness reaches 529 HV for series 1 and 592 HV for series 2. The factors increasing hardness and promoting martensite near the interface are firstly the cooling rate, which is always very high for the SLM process, and secondly the iron content, which is greater for series 2 in all cases. Thus, the hardness in the transition zone is always greater for series 2. In the case of 4 and 5 layers of the series 2, because combined effect of quenching induced by a sufficient cooling rate after laser heating with the presence of high iron content, martensite is present up to the coating surface without any transition zone and the hardness is greater.

Comparing the two manufacturing conditions of series 1 and 2 (Fig. 14), when the coating surface presents only one FCC phase, series 2 has a slightly lower microhardness because the iron content is higher than series 2 than for series 1. For a cobalt-based coating, the literature confirms that iron decreases the hardness of the FCC metastable phase [41].

To understand the microhardness variation in the coating thickness (Fig. 13) and the difference in its evolution between series 1 and series 2, this property must be correlated with both the crystalline phases and the changes that occur in the chemical composition. In [39] Zhang et al. obtained the same shaped hardness evolution curve as that found in the present work (9 layers). They obtained high hardness in the transition zone in their work. However, Zhu et al. demonstrate in [40] that hardness increases directly from substrate to coating and becomes constant without any higher hardness transition zone (as in the 4 layers of series 2).

## 5. Conclusions

In this study, CoCrMo coatings are applied by the SLM process to a C35 steel substrate. The aim of this experimental work was to study the dilution content of iron from the substrate to the coating and its influence on the crystalline phases and microhardness properties. Two parameters were investigated: the number of layers of coating and the interlayer time, which is the laser pass interval time between two successive layers.

Between the two fabrications (series 1 and series 2) only the interlayer time varies. All other parameters, i.e. scanning speed, laser power, rotation angle between layers, etc., are the same and the values used are those recommended by the SLM machine manufacturer. It can be observed that for the second layer in the case of series 1 the interlayer time is 42 s while in the case of series 2 the interlayer time is only 11 s. In the present work, it is found that this difference has a great influence on the heat flux which is tracked through by the iron dilution in the coating thickness.

The main contributions presented are as follows:

- The diluted iron content in the coating is higher with a low interlayer time, because reducing interlayer time increases the maximum temperature reached during laser melting layer by layer. On the other hand, iron content decreases with the number of layers. Consequently, the dilution of iron up to the surface drops to very low value, less than 10% in weight, from 5 layers of coating for an extended interlayer time, but from 9 layers of coating for a reduced interlayer time.
- The cooling rate is very high for the SLM process, and the dilution of the iron content becomes more significant when the interlayer time is reduced, inducing a high rate of martensite BCT structure called α'BCC and indicated by BCC peaks in the XRD pattern. In this case, the hardness of martensite is very high, up to 750HV. The mean coating microhardness decreases and the coating remains single phase FCC with a high content of iron and slightly increases when its iron content is reduced.
- For a high diluted iron content exceeding 45% in weight, a nonequilibrium crystalline system is created in the coating surface, with two different phases, FCC and α'BCC. Both phases represent substitutional solid solutions of iron in cobalt or cobalt in iron. In the cross section, it is observed that both phases have two different chemical compositions, including the iron content. Thus, regardless of interlayer time, the resulting crystalline system for the coating, except for a small residual HCP phase, is a totally out-of-equilibrium system with both FCC and/or α'BCC.
- The real coating thickness is always greater when the interlayer time is reduced.

## CRediT authorship contribution statement

This work is realized at Institut Clément Ader in IMT Mines Albi. Tarek Younsi is doctor who defended his thesis on March 2022. Christine BOHER and Adriana SOVEJA are supervisors. The article constitutes one part of thesis work. CRediT author statement: Tarek YOUNSI: Investigation, Writing Original Draft Christine BOHER: Supervision Adriana SOVEJA: Supervision.

## Declaration of Competing Interest

The authors declare that they have no known competing financial interests or personal relationships that could have appeared to influence the work reported in this paper.

## References


[1] C.T. Sims, N.S. Stoloff, W.C. Hagel, Superalloys II, J. Wiley & Sons, New York Chichester Brisbane (etc), 1987.
[2] G.F. Vander Voort, Metallography and Microstrocture. V9. ASM Handbook, ASM International, Materials Park, Ohio, 2004, pp. 762–773.
[3] E. Cabrol, C. Boher, V. Vidal, F. Rézaï-Aria, F. Touratier, Plastic strain of cobalt-based hardfacings under friction loading, Wear vol. 330–331 (2015) 354–363, doi: 10.1016/j.wear.2015.01.082.
[4] Š. Houdková, Z. Pala, E. Smazalová, M. Vostřák, Z. Česánek, Microstructure and sliding wear properties of HVOF sprayed, laser remelted and laser clad Stellite 6 coatings, Surf. Coat. Technol. vol. 318 (2017) 129–141, https://doi.org/10.1016/j.surfcoat.2016.09.012.
[5] V. Ocelík, U. de Oliveira, M. de Boer, J.T.M. de Hosson, Thick Co-based coating on cast iron by side laser cladding: analysis of processing conditions and coating properties, Surf. Coat. Technol. vol. 201 (n° 12) (2007) 5875–5883, https://doi.org/10.1016/j.surfcoat.2006.10.044.
[6] J. Tuominen, et al., Fatigue behavior of laser clad round steel bars, J. Laser Appl. vol. 27 (n° 1) (2014), 012006, https://doi.org/10.2351/1.4903351.
[7] K. Graf, et al., Effect of dilution on the microstructure and properties of CoCrMoSi alloy coatings processed on high-carbon substrate, Mater. Res. vol. 22 (1) (2019) doi: 10.1590/1980-5373-mr-2018-0502.
[8] L.-Y. Tian, R. Lizárraga, H. Larsson, E. Holmström, L. Vitos, A first principles study of the stacking fault energies for fcc Co-based binary alloys, Acta Mater. vol. 136 (2017) 215–223, https://doi.org/10.1016/j.actamat.2017.07.010.
[9] A. Cornet, F. Hlawka, Propriétés et comportements des matériaux: du microscopique au macroscopique, Ellipses, Paris, 2010. Nouvelle édition.
[10] C.Y. Yap, et al., Review of selective laser melting: materials and applications, Appl. Phys. Rev. vol. 2 (2015), 041101, https://doi.org/10.1063/1.4935926.
[11] T.V. Tarasova, A.P. Nazarov, M.V. Prokof'ev, Effect of the regimes of selective laser melting on the structure and physicomechanical properties of cobalt-base superalloys, Phys. Met. Metallogr. vol. 116 (n° 6) (2015) 601–605, https://doi.org/10.1134/S0031918×15060101.

[12] C. Song, M. Zhang, Y. Yang, D. Wang, Y. Jia-kuo, Morphology and properties of CoCrMo parts fabricated by selective laser melting, Mater. Sci. Eng. A vol. 713 (2018) 206–213, https://doi.org/10.1016/j.msea.2017.12.035.
[13] E. Liverani, et al., Fabrication of Co–Cr–Mo endoprosthetic ankle devices by means of Selective Laser Melting (SLM), Mater. Des. vol. 106 (2016) 60–68, https://doi.org/10.1016/j.matdes.2016.05.083.
[14] A. Takaichi, et al., Microstructures and mechanical properties of Co–29Cr–6Mo alloy fabricated by selective laser melting process for dental applications, J. Mech. Behav. Biomed. Mater. vol. 21 (2013) 67–76, https://doi.org/10.1016/j.jmbbm.2013.01.021.
[15] K. Darvish, Z.W. Chen, M.A.L. Phan, T. Pasang, Selective laser melting of Co-29Cr-6Mo alloy with laser power 180–360W: cellular growth, intercellular spacing and the related thermal condition, Mater. Charact. vol. 135 (2018) 183–191, https://doi.org/10.1016/j.matchar.2017.11.046.
[16] J.-H. Wang, J. Ren, W. Liu, X.-Y. Wu, M.-X. Gao, P.-K. Bai, Effect of selective laser melting process parameters on microstructure and properties of Co-Cr alloy, Materials vol. 11 (n° 9) (2018), https://doi.org/10.3390/ma11091546.
[17] H. Wang, J. Xu, Z. NIE, W. Ma, Q. Zhang, L. Guo, Preparation and properties of Co–Cr alloy denture by selective laser melting, Mater. Res. Express vol. 6 (n° 2) (2018), 026552, https://doi.org/10.1088/2053-1591/aaee5d.
[18] B. Qian, K. Saeidi, L. Kvetková, F. Lofaj, C. Xiao, Z. Shen, Defects-tolerant Co-Cr-Mo dental alloys prepared by selective laser melting, Dent. Mater. vol. 31 (n° 12) (2015) 1435–1444, https://doi.org/10.1016/j.dental.2015.09.003.
[19] Y. Kajima, et al., Fatigue strength of Co-Cr-Mo alloy clasps prepared by selective laser melting, J. Mech. Behav. Biomed. Mater. vol. 59 (2016) 446–458, 10.1016/j.jmbbm.2016.02.032.
[20] M. Cloots, K. Kunze, P.J. Uggowitzer, K. Wegener, Microstructural characteristics of the nickel-based alloy IN738LC and the cobalt-based alloy Mar-M509 produced by selective laser melting, Mater. Sci. Eng. A vol. 658 (2016) 68–76, https://doi.org/10.1016/j.msea.2016.01.058.
[21] C. Tan, K. Zhou, W. Ma, L. Min, Interfacial characteristic and mechanical performance of maraging steel-copper functional bimetal produced by selective laser melting based hybrid manufacture, Mater. Des. vol. 155 (2018) 77–85, https://doi.org/10.1016/j.matdes.2018.05.064.
[22] K. Chen, Y. Zou, B. Ma, H. Cu, F. Lub, P.X, Selective laser melting 316L/CuSn10 multi-materials: Processing optimization, interfacial characterization and mechanical property, J. Mater. Process. Technol. vol. 283 (2020), 116701 doi: 10.1016/j.jmatprotec.2020.116701.
[23] G. Mohr, S.J. Altenburg, K. Hilgenberg, Effects of inter layer time and build height on resulting properties of 316L stainless steel processed by laser powder bed fusion, Addit. Manuf. vol. 32 (2020), 101080, https://doi.org/10.1016/j.addma.2020.101080.
[24] T.M. Wischeropp, C. Emmelmann, M. Brandt, A. Pateras, Measurement of actual powder layer height and packing density in a single layer in selective laser melting, Addit. Manuf. vol. 28 (2019) 176–183, https://doi.org/10.1016/j.addma.2019.04.019.
[25] H.W. Mindt, M. Megahed, N.P. Lavery, M.A. Holmes, S.G.R. Brown, Powder bed layer characteristics: the overseen first-order process input, Met. Mat. Trans. A vol. 47 (n° 8) (2016) 3811–3822, https://doi.org/10.1007/s11661-016-3470-2.
[26] C. dos Santos, A.F. Habibe, B.G. Simba, J.F. Cardoso Lins, B.X. de Freitas, C. A. Nunes, CoCrMo-base alloys for dental applications obtained by selective laser melting (SLM) and CAD/CAM milling, Mater. Res. Ibero-Am. J. Mater. vol. 23 (2) (2020), e20190599 doi: 10.1590/1980-5373-MR-2019-0599.
[27] J.R. Davis, Nickel, Cobalt, and Their Alloys, ASM International, Materials Park, OH, 2000.
[28] E.-U. Battelle memorial institute, Cobalt monograph. Bruxelles: Centre d'information du cobalt, 1960.
[29] M.E. Wieser, et al., Atomic weights of the elements 2011 (IUPAC Technical Report), Pure Appl. Chem. vol. 85 (n° 5) (2013) 1047–1078, https://doi.org/10.1351/PAC-REP-13-03-02.
[30] S. Sun, M. Brandt, M. Easton, 2 - Powder bed fusion processes: an overview, in: M. Brandt (Ed.), Laser Additive Manufacturing, Woodhead Publishing, 2017, pp. 55–77, https://doi.org/10.1016/B978-0-08-100433-3.00002-6.
[31] J. Chen, Y. Yang, C. Song, M. Zhang, S. Wu, D. Wang, Interfacial microstructure and mechanical properties of 316L /CuSn10 multi-material bimetallic structure fabricated by selective laser melting, Mater. Sci. Eng. A vol. 752 (2019) 75–85, https://doi.org/10.1016/j.msea.2019.02.097.
[32] Y. Liu, J. Zhang, Z. Pang, Numerical and experimental investigation into the subsequent thermal cycling during selective laser melting of multi-layer 316L stainless steel, Opt. Laser Technol. vol. 98 (2018) 23–32, https://doi.org/10.1016/j.optlastec.2017.07.034.
[33] W. Kurz. Fundamentals of Solidification, fourth revised ed., Trans Tech Publications, Zurich, 1998.
[34] Q. Chen, G. Guillemot, C.-A. Gandin, M. Bellet, Numerical modelling of the impact of energy distribution and Marangoni surface tension on track shape in selective laser melting of ceramic material, Addit. Manuf. vol. 21 (2018) 713–723, https://doi.org/10.1016/j.addma.2018.03.003.
[35] S. Mrowec, Defects and diffusion in solids: an introduction, Elsevier PWN, Amsterdam Oxford New york Warszawa, 1980.
[36] J. Crank, E.P.J. Crank, The Mathematics of Diffusion, Clarendon Press, 1979.
[37] Z. Luo, Y. Zhao, Efficient thermal finite element modeling of selective laser melting of Inconel 718, Comput. Mech. vol. 65 (n° 3) (2020) 763–787, https://doi.org/10.1007/s00466-019-01794-0.
[38] M. Rahm, R. Hoffmann, N.W. Ashcroft, Corrigendum: atomic and ionic radii of elements 1–96, Chem. A Eur. J. vol. 23 (n° 16) (2017), https://doi.org/10.1002/chem.201700610.
[39] L. Zhang, C. Wang, L. Han, C. Dong, Influence of laser power on microstructure and properties of laser clad Co-based amorphous composite coatings, Surf. Interfaces vol. 6 (2017) 18–23, https://doi.org/10.1016/j.surfin.2016.11.006.
[40] Y.Y. Zhu, et al., High power diode laser cladding of Fe–Co–B–Si–C–Nb amorphous coating: layered microstructure and properties, Surf. Coat. Technol. vol. 235 (2013) 699–705, https://doi.org/10.1016/j.surfcoat.2013.08.050.
[41] R.G. Bohatch, et al., Influence of processing on the microstructure and properties of CoCrMoSi Alloy PTA coatings, Soldag. Insp. vol. 20 (n° 2) (2015) 219–227, https://doi.org/10.1590/0104-9224/SI2002.09.